Draft: Constraints on Simplified Dark Matter Models using Mono-X Collider Searches

Amelia J. Brennan,[a,1] **Millie F. McDonald,**[a] **Johanna Gramling**[b] **and Thomas Jacques**[b]

[a] *The University of Melbourne, Parkville 3010, Australia*

[b] *Université de Genève, Quai E. Ansermet 24, 1211 Genève 4, Switzerland*

  E-mail: a.brennan@student.unimelb.edu.au,
milliem@student.unimelb.edu.au, johanna.gramling@cern.ch,
thomas.jacques@sissa.it

ABSTRACT: The use of simplified models of dark matter is becoming increasingly prevalent in collider searches, and while early Run II results are beginning to appear, we look to see what further information can be extracted from Run I results. We consider three 'standard' simplified models that couple quarks to fermionic singlet dark matter: an s-channel vector mediator with vector or axial-vector couplings, and a t-channel scalar mediator. Upper limits on the couplings are calculated, and compared across three alternate channels, namely, mono-jet, mono-Z (leptonic) and mono-W/Z (hadronic). The strongest limits are observed in the mono-jet channel, however the computational simplicity, and absence of significant t-channel model width effects, in the mono-boson channels make these a straightforward and fast alternative.

---

[1]Corresponding author.

Contents

1 Introduction

Simplified models have emerged as a powerful tool for the interpretation of collider, direct and indirect detection signals of dark matter (DM). Previously, searches for DM were conducted within the context of both Effective Field Theories (EFTs) [1, 4, 5, 7, 32, 33] and full UV-complete theories such as Supersymmetry [8, 10–12, 40]. The latter approach, though well-motivated, is typified by a broad parameter space and generally yields results which are insensitive to the wider class of DM models. EFT constraints, in comparison, are applicable to a broad range of models and rely on the specification of only a small set of parameters, namely the suppression scale, $M_\star$, and the DM mass, m_{DM} [25]. In the EFT framework, interactions between the dark and Standard Model (SM) sector are parametrised by a set of higher-dimensional effective operators, that arise when the mass of the mediating particle is assumed to be significantly larger than the momentum transferred in a given interaction. Where this is not the case, the EFT prescription can produce constraints which detour dramatically from those of the associated UV-complete model [24–28]. This is not so important in direct detection experiments where the momentum transferred in the scattering of DM particles with heavy nuclei is generally of the order of tens of keV [13, 14], or in indirect searches where the annihilations of non-relativistic DM particles in the galactic halo occur with momentum transfers of order m_{DM} []. However, for hadron collider searches - where the accessible center of mass energy of two colliding baryons may be sufficient to produce the mediator on-shell - the range of validity of the EFT prescription is significantly diminished. Indeed, recent works have shown the EFT approach to be unreliable in certain cases for the interpretation of data collected during the $\sqrt{\hat{s}} = 8$ TeV Run I of the Large Hadron Collider (LHC) [15–17]. In light of this, simplified models have become the preferred tool for the interpretation of collider DM searches [18, 31, 52, 54, 55].

In a nutshell, a simplified model (SiM) arises when the heavy mediator which was integrated out in the EFT framework is reintroduced. Like EFTs, SiMs admit the comparison of results obtained in the different avenues of dark matter study [] and are defined by a relatively small set of parameters - namely m_{DM}, the mass of the mediator M_{med}, and the SM-mediator and DM-mediator coupling strengths, g_q and g_χ (or $g_{q\chi}$ in the case of a single, SM-DM-mediator coupling). Unlike EFTs, constraints calculated within the context of a SiM are valid across a broad energy range.

In this paper, we examine a phenomenologically distinct set of SiMs. In particular, we place constraints on the SiMs corresponding to the simplest UV-completions of the D5 (vector) and D8 (axial-vector) effective operators in the s-channel[1]. We also include a case in which a scalar mediator is exchanged in the t-channel, motivated by its analog of squark

---

[1]The D5 and D8 operators form a nice starting point in the analysis of simplified models as they have been studied exhaustively in the past (see refs. [1, 4, 5, 7, 15–17, 32, 33] among others). This attention is motivated by the fact that collider limits for the D5 (D8) operator can be readily transformed into limits on spin-independent (spin-dependent) DM-nucleon scattering and vice versa. With the exception of D1 (see sec. **??**), and D9 and D11 (which have no simple simplified model counterparts []), the remaining effective operators induce elastic scattering which is suppressed by powers of the DM velocity or the momentum transferred [19]. Hence, these operators are not often considered in the literature.

exchange in Supersymmetry. In the heavy mediator limit, this model is converted into a combination of the D5 and D8 EFTs via a Fierz transformation.

The models are constrained using public results from mono-X + missing transverse energy (E_T^{miss}) searches conducted by the ATLAS Collaboration. Specifically we focus on searches where X is either a parton (manifesting in the detector as a narrow-radius jet), a leptonically-decaying Z boson, or a hadronically-decaying W or Z boson (manifesting as a large-radius jet). The purpose of this work is to strengthen existing SiM limits [23, 56] using the full 20.3 fb^{-1} of Run I ATLAS data, and to explore an enhanced phase space with respect to the mediator and DM masses and the relative strength of the couplings to the visible and dark sectors. We choose to treat the mediator width as the minimal value naturally arising, as an alternative to many past analyses which handle this as a fixed value []. We extend the study by providing a cross-check and comparison of the performance of the three targeted collider detection channels, and compare against relic density and direct detection constraints.

The remainder of the paper is organised as follows. Section 2 contains a compendium of the SiMs chosen for analysis and the associated collider phenomenology. Section 3 outlines the techniques used to recast mono-X + E_T^{miss} limits on the visible cross-section for any new physics process into constraints on SiMs, and specifically on the couplings g_q and g_χ. Lastly, our results are presented in Section 4 along with a discussion of the implications of this work. Appendices A and B include details of the limit setting and analysis validation procedures.

2 Simplified Model Phenomenology

2.1 Model Descriptions

We begin with a short set of assumptions: that the DM particle, χ, is a weakly interacting Dirac fermion, that it is a singlet under the SM, and that it is the lightest stable new particle. Additionally the new sector is assumed to couple only to the SM quarks; while possible coupling to SM leptons [] or gluons [] has been studied elsewhere, it is beyond the scope of this paper. The nature of the mediating particle then results from these assumptions: in the s-channel it is chosen to be a vector particle and so must also be a SM singlet, denoted ξ, while in the t-channel it is identified as scalar and is necessarily charged and coloured, and labelled ϕ.

The s-channel models chosen for analysis are characterised by vector (sV) or axial-vector (sA) couplings to both the dark and SM sectors. They are described by the following interaction Lagrangians:

$$\mathcal{L}_{sV} = -\xi_\mu \left[\sum_q g_q \bar{q} \gamma^\mu q - g_\chi \bar{\chi} \gamma^\mu \chi \right], \tag{2.1}$$

$$\mathcal{L}_{sA} = \xi_\mu \left[\sum_q g_q \bar{q} \gamma^\mu \gamma_5 q - g_\chi \bar{\chi} \gamma^\mu \gamma_5 \chi \right], \tag{2.2}$$

where the sum is over all quarks. For the couplings g_q and g_χ to remain within the perturbative regime, they are required to satisy $g_q, g_\chi \leq 4\pi$, though stronger perturbativity requirements do exist [15].

The t-channel model considered in this paper (abbreviated tS) is characterised by a scalar mediator and is motivated by analogy with a common aspect of Supersymmetric models: neutralino DM interacting with the SM sector via t-channel exchange of a squark [20]. Note that in this Supersymmetric scenario the DM particle is a Majorana fermion. SiMs in which χ is of Majorana type are kinematically identical to the corresponding Dirac cases (requiring multiplication of the cross-section by a simple factor in order to compute limits) and so are not covered here[2]. The exception to this rule is the s-channel vector mediator model, which vanishes if χ is a Majorana fermion [21].

In the tS model, the mediator is allowed to couple to either the left or right-handed quarks as an SU(2) doublet or singlet respectively. Since the LHC is insensitive to the chirality of the quarks, we assume for simplicity that ϕ couples to the left-handed quarks only, and is itself an SU(2) doublet. To avoid coupling quarks of different generations, and to remain in step with the DM forum recommendations [], we include three generations of mediator ϕ, with equal masses and couplings. The interaction Lagrangian for this model is then:

$$\mathcal{L}_{tS} = \sum_Q g_{q\chi} \bar{Q} P_R \phi \chi + \text{h.c.}, \qquad (2.3)$$

where the sum is over the three Q_L doublets, $g_{q\chi}$ is the scalar coupling of the incoming quark, ϕ and χ, and P_R is the usual chiral projection operator.

2.2 The Mono-X + E_T^{miss} Signature

The mono-X + E_T^{miss} (abbreviated to mono-X) is a popular collider signal in the search for new physics, particularly in the search for dark matter. Since DM particles are not expected to interact with detector material, they appear as missing transverse energy when balanced against a visible object, X, that is radiated from the initial or intermediate state (where the latter is permitted in the t-channel model) [?]. For the s-channel SiMs discussed above, only initial-state radiation is permitted; see figs. 1a and 1b for examples. For the tS model, radiation of a gluon or electroweak (EW) boson is permitted both from initial state partons (fig. 1c) or from the mediator (fig. 1d).

~~To fully exploit the potential of the ATLAS detector to record and identify a vast array of particle types, we consider for analysis three scenarios: 1). X is a parton which hadronises to form a jet, 2.) X is a Z boson which decays into an $\ell^+\ell^-$ pair, and 3.) X is a hadronically-decaying W or Z boson. In the context of DM searches, these signatures are referred to as mono-jet, mono-Z, and mono-W/Z respectively. Note that the mono-jet scenario is the most likely scenario at the LHC owing to the strength of the strong coupling yet the mono-Z channel has the advantage of a relative simple and clean signature. OR: Leptons are in general much cleaner and simpler than jets, so this channel is included here to investigate whether the reduction in systematic uncertainties can provide easily-obtained~~

---

[2]The exception being in the validation of the mono-Z channel, see Sec. B.2.
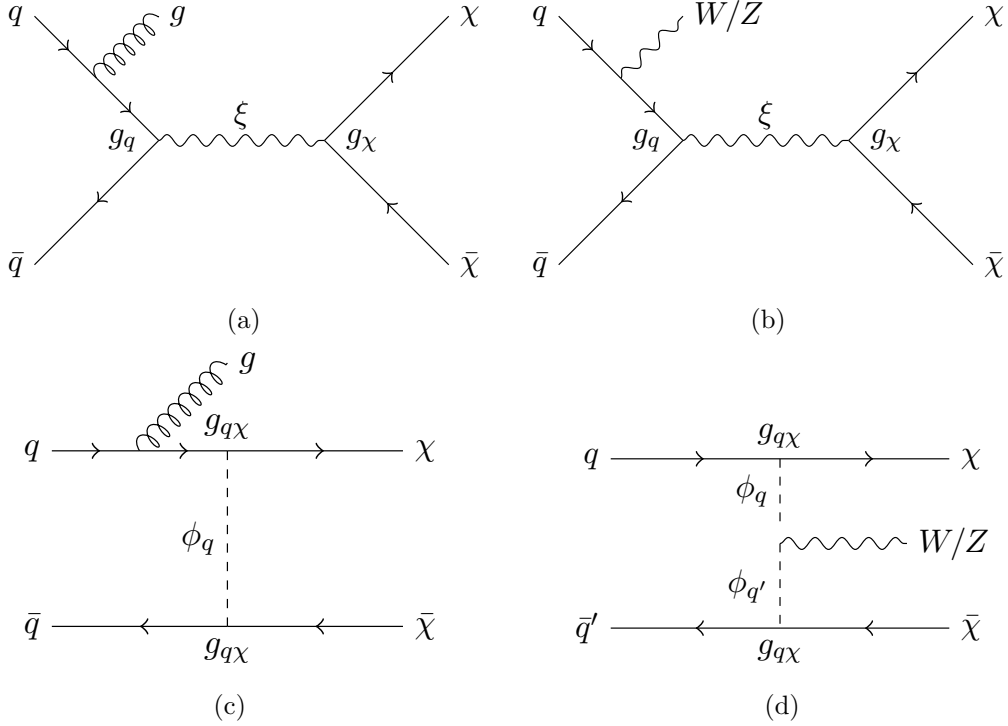
Figure 1: Representative dark matter pair-production processes with a gluon or W/Z boson in the final state for the s-channel (a,b) and t-channel (c,d) models.

~~results that are comparable to the more complicated mono-jet channel. The inclusion of the~~
~~mono-WZ channel is motivated by its fundamentally different signature structure wherein~~
~~event selection is based on large-R jets that are consistent with having come from an EW~~
~~boson.~~

NEW: The most likely scenario at the LHC is production of a jet alongside the invisible χ pair, as a result of the strong coupling and prevalence of partons in the initial state. However, to fully exploit the potential of the ATLAS detector to record and identify a vast array of particle types, we can include the alternative mono-W/Z channels to potentially glean further information. We can take advantage of the relative cleanliness and simplicity of leptons in the leptonically-decaying mono-Z channel, or the large hadronic branching fraction, and developing techniques to identify jets resulting from EW bosons, in the hadronically-decaying mono-W/Z channel. In both cases, the large multi-jet background is reduced, and complications in jet production such as parton-matching can be ignored, making these an interesting alternative where speed, efficiency and a reduction in jet-associated uncertainties may make up for the loss in sensitivity.

2.3 Mass and Coupling Points

A representative set of dark matter and mediator masses, listed in table 1, are chosen for study in each detection channel. DM masses of 3, 30 and 300 GeV were also included in the mono-Z channel, where ease of production can afford higher granularity. All $(m_\chi, M_{\mathrm{med}})$

m_χ [GeV]	M_{med} [GeV]	s-channel		t-channel
		g_q	g_χ	$g_{q\chi}$
1, (3), 10, (30), 100, (300), 1000	1, 2, 10, 20, 100, 200, 1000, 2000	1	0.2, 0.5, 1, 2, 5	1

Table 1: Mass and coupling points chosen for the analysis of simplified dark matter models. Values in brackets are only included in the mono-Z channel. The mediator masses are primarily representative of three regimes: (near-)degenerate ($M_{\mathrm{med}} \approx m_\chi$), on-shell ($M_{\mathrm{med}} \geq 2m_\chi$), and EFT-like ($\sqrt{\hat{s}} << M_{\mathrm{med}}$). For the t-channel model, $M_{\mathrm{med}} > m_\chi$ is also required.

combinations are permitted in the sV and sA models, while in the tS model M_{med} must be greater than m_χ to ensure stability of the DM particle. The couplings g_q and $g_{q\chi}$ are set to unity, while the DM-mediator coupling in the s-channel models, g_χ, was varied from 0.2 to 5. The mediator masses are chosen to cover a broad range of parameter space and to coincide with predominantly three regimes: (near-)degenerate ($M_{\mathrm{med}} \approx m_\chi$), on-shell ($M_{\mathrm{med}} \geq 2m_\chi$), and EFT-like ($\sqrt{\hat{s}} << M_{\mathrm{med}}$) [3]. We also allow for the possibility of a light mediator/heavy WIMP scenario ($M_{\mathrm{med}} < m_\chi$) in the sV and sA models.

2.4 Width Effects

An important factor when considering simplified models is to ensure the mediator width is treated appropriately, as it impacts both the cross-section calculation and, in some cases, the kinematic behaviour of the model. In previous analyses (ref) it has been common to consider mediators of a fixed width such as $\Gamma = M/8\pi$ (the minimal width possible with only a single quark helicity coupling to the mediator with $g_q = 1$), to take advantage of the enhancement in cross-section as the width becomes small and on-shell.

In this work, the mediator widths are expanded to include coupling to all kinematically accessible quarks. We assume minimal flavour violation, which implies a universal coupling to all quark flavours. Following [(other minimum width papers)], the minimum on-shell kinetic width for each model is given by:

$$
\begin{aligned}
\Gamma_{sV} = & \frac{g_\chi^2 M}{12\pi} \left(1 + \frac{2m_\chi^2}{M^2}\right) \left(1 - \frac{4m_\chi^2}{M^2}\right)^{\frac{1}{2}} \Theta(M - 2m_\chi) \\
& + \sum_q \frac{g_q^2 M}{4\pi} \left(1 + \frac{2m_q^2}{M^2}\right) \left(1 - \frac{4m_q^2}{M^2}\right)^{\frac{1}{2}} \Theta(M - 2m_q)
\end{aligned}
\tag{2.4}
$$

---

[3]A recent study by Alves et al. found that EFT results do not apply to mediators with a mass less than 2.5 TeV at the LHC during Run I [35].

$$\begin{aligned}
\Gamma_{sA} &= \frac{g_\chi^2 M}{12\pi}\left(1 - \frac{4m_\chi^2}{M^2}\right)^{\frac{3}{2}}\Theta(M - 2m_\chi) \\
&+ \sum_q \frac{g_q^2 M}{4\pi}\left(1 - \frac{4m_q^2}{M^2}\right)^{\frac{3}{2}}\Theta(M - 2m_q)
\end{aligned} \tag{2.5}$$

$$\begin{aligned}
\Gamma_{tS} &= \sum_q \frac{g_{q\chi}^2 M}{16\pi}\left(1 - \frac{m_q^2}{M^2} - \frac{m_\chi^2}{M^2}\right) \\
&\times \sqrt{\left(1 - \frac{m_q^2}{M^2} + \frac{m_\chi^2}{M^2}\right)^2 - 4\frac{m_\chi^2}{M^2}}\ \Theta(M - m_q - m_\chi)
\end{aligned} \tag{2.6}$$

The above expressions are valid where the width is smaller than the mass of the mediator.

A recent paper [Tom+Karl, others?] demonstrated that the generator treatment of the mediator as a Breit-Wigner propagator, rather than a true kinetic propagator, is accurate only up to $\Gamma \lesssim M/2$. This was also shown to be a necessary requirement for the following approximations to hold:

$$\sigma \propto \begin{cases} g_q^2 g_\chi^2/\Gamma & \text{if } M_{\text{med}} \geq 2m_{\text{DM}} \\ g_q^2 g_\chi^2 & \text{if } M_{\text{med}} < 2m_{\text{DM}} \end{cases} \tag{2.7}$$

in the sV and sA models, and

$$\sigma \propto g_{q\chi}^4 \tag{2.8}$$

in the tS model. When valid, these approximations allow us to greatly simplify our limit calculations.

To simplify the procedure further, we can take advantage of the fact that (with the notable exception of the tS model in the mono-jet channel) for each point in (m_χ, M_{med}) phase space, the mediator width (and therefore the couplings) do not greatly affect each model's kinematic behaviour. This is demonstrated in fig. 2, where for the sV (representing both the sV and sA models) and tS models, we plot a simplified E_T^{miss} distribution, as a proxy for the full selection in each analysis, for two mass points and a demonstrative set of couplings such that $\Gamma < M_{\text{med}}/2$. The E_T^{miss} distribution is predominantly independent of the mediator width for the s-channel models in the mono-jet channel, and all models in the mono-Z [4] channel. However, there is a clear variation in the kinematic behaviour of the tS model in the mono-jet channel, which can be attributed to additional diagrams (accessible only in this channel) featuring a gluon in the initial state and subsequently allowing the mediator to go on-shell. In this scenario, when the resulting quark and DM particle are

---

[4] In this discussion, the mono-W/Z channel can be assumed to follow the same logic as for the mono-Z channel.

Figure 2: The E_T^{miss} distribution of the sV and tS models in the mono-jet and mono-Z channels, for some demonstrative masses. The parameter μ is defined as Γ/M_{med}, and is used to demonstrate the impact of a changing width; in particular, the tS model in the mono-jet channel shows clear width-dependence. The widths are obtained with couplings of 0.1, 1, and 5 where $\mu < 0.5$ remains true.

214 both small compared to the mediator mass, they share equally its energy leading to a peak
215 in the E_T^{miss} distribution at approximately half the mediator mass.

216   In the cases where the model behaviour is independent of the width, we can greatly
217 simplify the calculations by assuming the impact of the selection cuts in each channel is
218 unchanged for each masspoint; that is, independent of the couplings. In this case, a simple
219 rearrangement of eqns. 2.7 and 2.8 allows us to obtain upper limits on the model couplings
220 (see App. A for further details of this calculation).

221   A proper study of the tS model within the mono-jet channel, where altering the cou-
222 pling can lead to changed kinematic behaviour, has been performed elsewhere [Papucci],
223 and requires the production of individual samples for each coupling point. This, combined
224 with the challenges associated with including differing orders of α_s, make the generation
225 process computationally expensive compared to the mono-Z and mono-W/Z channels. We
226 therefore exclude an analysis of the tS model in the mono-jet channel in this work.

3 Recasting mono-X constraints

The procedure for recasting existing mono-X analyses to obtain SiM constraints follows a simple cut-and-count methodology. Firstly, signal events are simulated (described below in section 3.1) with object p_T smearing applied to approximate the detection efficiency of the ATLAS detector, ϵ. The event selection criteria of the mono-X analysis of interest is then applied to the simulated signal samples. Events surviving the selection criteria are counted to determine the likelihood of a dark matter event being observed (referred to as the acceptance, $\mathcal{A}$), which is then used in combination with channel-specific model-independent limits on new physics events to limit the parameter phase space of a given model. For a comprehensive description of the recasting procedure, see appendix A.

In this paper, mono-jet constraints are derived from a search for new phenomena conducted by the ATLAS Collaboration using pp collisions at $\sqrt{s} = 8$ TeV as described in ref. [41]. Similarly, the leptonic mono-Z and hadronic mono-W/Z constraints are derived from ATLAS dark matter searches originally optimised for the D1, D5 and D9 effective operators [47**?**]. These analyses are described in further detail in sections 3.2, 3.3 and 3.4 respectively.

3.1 Signal Simulation

Monte Carlo simulated event samples are used to model the expected signal for each channel and for each simplified model. Leading order matrix elements for the process $pp \rightarrow X + \chi\bar{\chi}$ (where X is specifically one or two jets[5], a $Z(\rightarrow \ell^+\ell^-)$ boson or a $W/Z(\rightarrow jj)$ boson) are first simulated using MADGRAPH5_AMC@NLO v2.2.2 [48] with the MSTW2008lo68cl PDF [49]. During this stage, the renormalisation and factorisation scales are set to the default sum of $\sqrt{m^2 + p_T^2}$ for all particles in the final state. Showering and hadronisation are then performed by PYTHIA 8.201 [] with the appropriate PDF and using the ATLAS UE Tune AU2-MSTW2008LO [50]. Reconstruction of small-radius jets (from hereon referred to just as 'jets') for the mono-jet channel is performed by FastJet [] using the anti-k_T algorithm with radius parameter $R = 0.4$. Similarly, reconstruction of large-radius jets for the mono-W/Z channel is performed using the Cambridge-Aachen algorithm with $R = 1.2$. The latter channel also includes a mass-drop filtering procedure with $\mu = 0.67$ and $\sqrt{y}^6 = 0.4$ (see ref. [] for further details), which favours large-R jets with two balanced subjets, consistent with the decay of an EW boson to a (potentially-boosted) dijet pair. Lastly, the detector response is approximated by applying a Gaussian smearing factor to the p_T of all leptons and jets.

3.1.1 Parton Matching Scheme

In the ATLAS mono-jet analysis, matching of partons generated in MADGRAPH5 to jets generated in PYTHIA is performed using the MLM scheme, with two matching scales, or values of 'QCUT', per mass/coupling point. The QCUT values span a broad kinematic

---

[5]Jets are seeded by any parton excluding the (anti-)top quark.

[6]$\sqrt{y} = \min(p_{T_{j_1}}, p_{T_{j_2}})\Delta R / m_{jet}$ is the momentum balance of the two leading subjets.

₂₆₄ range in combination with a cut placed on the leading jet p_T per event to avoid double-
₂₆₅ counting. This treatment aims to mitigate the impact of the matching scale on the shape
₂₆₆ of the p_T and E_T^{miss} distributions; that is, to reduce the uncertainty in those areas of phase
₂₆₇ space where the mediator mass is significantly larger or smaller that the QCUT value.
₂₆₈ For the analysis of SiMs, we use instead a single matching scale of 80 GeV. Though not
₂₆₉ ideal, this approach suitably reproduces the results of the ATLAS mono-jet analysis for
₂₇₀ the masses of interest (see Sec. B.1). Importantly, it also reduces the complexity and
₂₇₁ computational expense involved in estimating limits for the mono-jet channel.

₂₇₂ We now move to a discussion of each of the mono-X channels separately.

3.2 Mono-jet Constraints

₂₇₄ The ATLAS mono-jet + E_T^{miss} analysis [41] was originally designed to set limits on three
₂₇₅ new physics scenarios, the most relevant of which is the production of WIMP DM within
₂₇₆ the context of seven (?) effective operators. The analysis also includes a brief study of a
₂₇₇ Z' DM model which is analogous to our sV model.

₂₇₈ Signal selection is carried out based on at least one hard jet recoiling against missing
₂₇₉ energy. To ensure that the correct back-to-back jet + E_T^{miss} topology is selected events are
₂₈₀ required to have a leading jet, j_1, with $p_T > 120$ GeV and $|\eta| < 2.0$ satisfying $p_T^{j_1}/E_T^{\text{miss}} >$
₂₈₁ 0.5. Surviving events must then satisfy $|\Delta\phi(j, \vec{E}_T^{\text{miss}})| > 1.0$, where j is any jet with $p_T >$
₂₈₂ 30 GeV and $|\eta| < 4.5$. This criterion reduces the multijet background contribution where
₂₈₃ the large E_T^{miss} originates mainly from jet energy mismeasurement. Note that there is no
₂₈₄ upper limit placed on the number of jets per event. The contribution from the dominant
₂₈₅ background processes, W/Z+jets , is managed with a veto on events containing muons or
₂₈₆ electrons with $p_T > 7$ GeV. A further veto is placed on events containing isolated tracks[7]
₂₈₇ with $p_T > 10$ GeV and $|\eta| < 2.5$, to reduce the contribution from non-identified leptons (e,
₂₈₈ μ or τ) in the final state. Lastly, nine separate signal regions are defined with increasing
₂₈₉ lower thresholds on E_T^{miss}, which range from 150 GeV to 700 GeV as shown in table 2.

₂₉₀ The ATLAS mono-jet analysis revealed no significant deviation of observed events
₂₉₁ from the expected SM backgrounds in the Run 1 8 TeV dataset. Subsequently, model-
₂₉₂ independent limits on new physics signatures were provided in terms of the visible cross-
₂₉₃ section, $\sigma \times \mathcal{A} \times \epsilon$; these are listed in table 2.

₂₉₄ The signal simulation procedure outlined in sec. 3.1 and implementation of the selec-
₂₉₅ tion criteria discussed above were validated for the mono-jet channel via reproduction of
₂₉₆ ATLAS limits on the suppression scale, $M_\star \equiv M_{\text{med}}/\sqrt{g_q g_\chi}$, for the Z' model. The details
₂₉₇ of this process are contained in appendix B.1. Importantly, we observe agreement within
₂₉₈ $\sim$12% for all samples.

3.3 Mono-Z Constraints

₃₀₀ The ATLAS mono-$Z(\to \ell^+\ell^-)$ + E_T^{miss} analysis [47] was principally designed to constrain
₃₀₁ a set of EFT models of DM. As a secondary focus, it also includes a short study of a

---

[7]A track is considered isolated when no additional track with $p_T > 3$ GeV lies within a cone of radius 0.4 around it.

Signal Region	E_T^{miss} threshold [GeV]	$\sigma \times \mathcal{A} \times \epsilon$ [fb]
SR1	150	726 (935)
SR2	200	194 (271)
SR3	250	90 (106)
SR4	300	45 (51)
SR5	350	21 (29)
SR6	400	12 (17)
SR7	500	7.2 (7.2)
SR8	600	3.8 (3.2)
SR9	700	3.4 (1.8)

Table 2: The ATLAS mono-jet E_T^{miss} signal regions and corresponding observed (expected) model-independent upper limits on $\sigma \times \mathcal{A} \times \epsilon$ at 95% confidence level. Adapted from Ref. [41].

302 *t*-channel simplified model similar to our *tS* model.

303 The selection criteria for this analysis are summarised as follows (see the paper for a
304 full description). Electrons (muons) are required to have a p_T greater than 20 GeV, and
305 $|\eta|$ less than 2.47 (2.5). Two opposite-sign, same-flavour leptons are selected, and required
306 to have invariant mass and pseudorapidity such that $m_{\ell\ell} \in [76, 106]$ GeV and $|\eta^{\ell\ell}| < 2.5$.
307 The reconstructed Z boson should be approximately back-to-back and balanced against
308 the E_T^{miss}, ensured with the selections $\Delta\phi(\vec{E}_T^{miss}, p_T^{\ell\ell}) > 2.5$ and $|p_T^{\ell\ell} - E_T^{miss}| / p_T^{\ell\ell} < 0.5$.
309 Events containing a jet with $p_T > 25$ GeV and $|\eta| < 2.5$ are vetoed. Events are also vetoed
310 if they contain a third lepton with $p_T > 7$ GeV. The signal regions are defined by increasing
311 lower E_T^{miss} thresholds: $E_T^{miss} > 150, 250, 350, 450$ GeV.

312 A cut-and-count strategy is used to estimate the total observed yields and expected SM
313 backgrounds in each signal region. The limits on $\sigma \times \mathcal{A} \times \epsilon$ are not publicly available, so we
314 take the numbers of expected and observed events, along with the associated uncertainties,
315 and convert these into model-dependent upper limits with a single implementation of the
316 HistFitter framework [53] using a frequentist calculator and a one-sided profile likelihood
317 test statistic (the LHC default). The results of this process are displayed in table 3. Note
318 that we use signal regions 1 and 2 only, as our simplified HistFitter approach is inadequate
319 to handle the very low statistics of signal regions 3 and 4. These upper limits are also used
320 for the validation of the mono-Z signal generation and selection procedures (see app. B.2).

3.4 Mono-W/Z Constraints

322 The ATLAS mono-$W/Z + E_T^{miss}$ search [] was originally aimed at constraining the spin-
323 independent effective operators C1, D1, and D5, and the spin-dependent D9. The search
324 was originally designed to exploit the constructive interference of W boson emission from
325 opposite-sign up-type and down-type quarks, leading to DM production wherein the mono-
326 W channel is dominant. Recent studies [] have revealed this scenario to violate unitarity
327 and so we ignore it in this analysis.

Signal Region	$E_\mathrm{T}^\mathrm{miss}$ threshold [GeV]	$\sigma \times \mathcal{A} \times \epsilon$ [fb]
SR1	150	1.59 (1.71)
SR2	250	0.291 (0.335)

Table 3: The ATLAS mono-Z $E_\mathrm{T}^\mathrm{miss}$ signal regions and corresponding observed (expected) model-independent upper limits on $\sigma \times \mathcal{A} \times \epsilon$ at 95% confidence level. Adapted using HistFitter from ref. [47].

The mono-W/Z event selection is carried out as follows. Large-radius jets are selected using a mass-drop filtering procedure (see sec. 3.1) to suppress non-W/Z processes. Events are required to contain at least one large-R jet with $p_\mathrm{T} > 250$ GeV, $|\eta| < 1.2$ and a mass, m_jet, within a 30-40 GeV window of the W/Z mass (i.e. $m_\mathrm{jet} \in [50, 120]$ GeV). In order to reduce the $t\bar{t}$ and multijet backgrounds, a veto removes events containing a small-R jet with $\Delta\phi(\mathrm{jet}, E_\mathrm{T}^\mathrm{miss}) < 0.4$, or containing more than one small-R jet with $p_\mathrm{T} > 40$ GeV, $|\eta| < 4.5$, and $\Delta R(\text{small-}R \text{ jet, large-}R \text{ jet}) > 0.9$. Electrons, muons and photons are vetoed if their p_T is larger than 10 GeV and they lie within $|\eta| < 2.47$ (electrons), 2.5 (muons), 2.37 (photons). Two signal regions are defined with $E_\mathrm{T}^\mathrm{miss} > 350$ GeV and $E_\mathrm{T}^\mathrm{miss} > 500$ GeV. Note that, in the recasting procedure, we consider only the second signal region (see Sec. **??** for further details). (should have a statement explaining this choice).

The ATLAS analysis used a shape-fit of the mass distribution of the large-R jet to estimate the background yields in the two signal regions, along with the associated statistical and systematic uncertainties. As in the mono-Z case, we convert these values into upper limits on the expected and observed number of new physics events using the HistFitter framework. For the $E_\mathrm{T}^\mathrm{miss} > 500$ GeV signal region, we obtain the limits shown in table 4.

Signal Region	$E_\mathrm{T}^\mathrm{miss}$ threshold [GeV]	$\sigma \times \mathcal{A} \times \epsilon$ [fb]
SR2	500	1.35 (1.34)

Table 4: The ATLAS mono-W/Z $E_\mathrm{T}^\mathrm{miss}$ signal region considered in this work and corresponding observed (expected) model-independent upper limits on $\sigma \times \mathcal{A} \times \epsilon$ at 95% confidence level. Adapted using HistFitter from ref. [].

4 Limits on the coupling $\sqrt{g_q g_\chi}$

The 95% confidence level upper limits on the sV and sA model couplings, $\sqrt{g_q g_\chi}$, and the tS model coupling, $g_{q\chi}$, which are obtained from each of the mono-X channels, are presented in figs. 3 - 8. These quantities were evaluated as described in appendix A and correspond to the best limits of each signal region tested.

In each plot, the grey region represents the phase space where no meaningful limit was obtained, that is, where the limit of at least one of the couplings was found to be greater

than 4π (and thus well out of the perturbative region). The white (hatched) regions coincide with those mass points which yield an initial (final) value of $\sqrt{g_q g_\chi}$ which fails to satisfy $\Gamma < M_{\mathrm{med}}/2$. Note that only the mono-jet channel produced limits which survive this requirement when $g_\chi/g_q = 0.2$, as shown in fig. 7. We subsequently omit the plots containing the associated limits for the mono-Z and mono-W/Z channels.

We note here that values of $\sqrt{g_q g_\chi}$ and $g_{q\chi}$ smaller than our hard upper limit of 4π, beyond which any results are considered meaningless, may also become increasingly invalid as they become less perturbative. Additionally, values for which the width is just within our upper validity bound of $M_{\mathrm{med}}/2$ may be pushed over into the invalid range with the addition of new particles, not considered here, which would serve to increase the mediator width.

Large DM masses: small cross sections, limited by ATLAS analysis optimisation, requires more data or further optimisation. Small DM masses: have low $E_{\mathrm{T}}^{\mathrm{miss}}$, would require more statistics. (True for mono-Z and I assume monojet also.)

The results are discussed according to channel below.

4.1   Mono-jet channel

The upper limits on the coupling combination $\sqrt{g_q g_\chi}$ (calculated at 95% confidence interval) of the sV and sA models, obtained in the mono-jet channel, are displayed in the left-hand column of figs. **??**, for $g_q/g_\chi = 0.5$, 1, 2 and 5 respectively. Additional results for the $g_q/g_\chi = 0.2$ case are also shown separately in fig. 7, as these limits are only meaningful within the mono-jet channel.

Examining first the sV model, we see stronger limits in the region of phase space where $M_{\mathrm{med}} > m_\chi$ (why?), and weaker limits where $M_{\mathrm{med}} < m_\chi$ (due to small cross sections). The weakest limits result for large m_χ or large M_{med}, and in fact are so weak that they are pushed into the region of invalidity where $\Gamma > M_{\mathrm{med}}/2$; this is because although the acceptance is considerably higher in these regions compared to low masses, the cross section is sufficiently small that this effect prevails. Within the valid region ($m_\chi \in [1, 100]$ GeV and $M_{\mathrm{med}} \in [1, 200]$ GeV), the limit on $\sqrt{g_q g_\chi}$ generally ranges from 0.1 to 0.7, with a handful of on-shell masses reaching a limit of $\sim$0.05 in the large g_χ/g_q case.

As the ratio g_χ/g_q varies, the coupling limits tend to remain approximately constant, as is expected when the coupling (and hence the width) has been demonstrated to have little effect on kinematic behaviour (and using the assumptions of eq. 2.7). As the ratio increases, points in the region $M_{\mathrm{med}} > m_\chi$ disappear as the initial condition, $g_q = 1$, leads to failure of the width condition. However, one could easily have chosen a smaller initial value of g_q to recover these points, and we suggest that the limits in this region would be quite similar to those seen in the $g_\chi/g_q = 0.2$ and 0.5 cases.

In the large ratio scenario, limits for $m_\chi = 1000$ GeV start to become valid. This is because if $\sqrt{g_q g_\chi}$ remains constant but the g_χ/g_q increases then the value of g_q is pushed downward and so the width, which is dominated by decays to SM particles, decreases.

The uncertainties on the limits displayed here generally range from ??% to ??%, and are dominated by X.

– 13 –

Moving next to the sA model within this channel, we find that the strongest limits are obtained when $m_\chi > M_{\mathrm{med}}$, thanks to both an improved acceptance and a higher cross section. Similarly to the sV model, as the couplings ratio increases, the limit remains approximately constant, and the high m_χ points move back into the valid region. The uncertainties for this model are dominated by X and are within the range $X \sim Y\%$.

4.2 Mono-Z channel

The simplicity of the mono-Z channel relative to the mono-jet channel, and the speed of its production within MADGRAPH5, allowed us to study a finer granularity of points in the mass phase space. The resulting limits on the sV and sA models are shown in the central column of figs. **??**. The behaviour of the limits as g_χ/g_q varies is similar to that within the mono-jet channel, and overall the limits are weaker compared to that channel by a factor of a few.

The total relative uncertainties on $\sqrt{g_q g_\chi}$ are generally within 10%, but can range up to 80% in a few cases.

The advantage of the mono-boson channels is in the study of the tS model; since this was not included in the mono-jet channel the strongest limits are obtained with the mono-Z analysis, and are shown in the left-hand side of fig. 8. In general the tS model limits are weaker than the corresponding s-channel points (why?), note that the scale here is increased by a factor of 10. We find stronger limits for smaller m_χ and M_{med} masses, where larger cross sections compensate for lower acceptances at these points.

4.3 Mono-W/Z channel

The limits on the couplings of the sV, sA and tS models, obtained within the mono-W/Z channel, are shown in the right-hand column of figs. **??**. This channel was studied to compare with the leptonic mono-Z channel in particular, but a coarser selection of masses was chosen as the limits were initially found to be somewhat weaker. Additionally, further estimates were made: a) as the kinematic behaviour is reasonable independent of the couplings, a single acceptance was found for each (m_χ, M_{med}) combination and applied to each value of g_χ/g_q, and b) complete systematic uncertainties were generated for a subset of masses and compared to those from the mono-Z channel; from this comparison the mono-Z systematic uncertainties were multiplied by 3 and then applied to the mono-W/Z limits. As a result, the limits obtained in this channel are not intended to be rigorously testable; rather, they are used more to indicate qualitatively how the channel compares.

The ATLAS mono-W/Z analysis was not optimised for a simplified model interpretation, and much of the phase space produced insignificant numbers of events passing the event selection, with up to 200 thousand events generated. Generally, the limits are a factor of a few weaker again than those from the mono-Z channel, which is both consistent with the limits on the EFT models studied in the ATLAS analyses, and expected following the use of a cut-and-count interpretation of the mono-W/Z public results (can we say this? Point is to compare with them probably doing a shape analysis to improve their limits). Some exceptions do exist however - the low-M_{med} region of the sA model shows limits comparable to those within the mono-Z channel.

Overall, the uncertainties from this channel lie within the range XXX.

5 Conclusion

5.1 Comparison with Relic Density Constraints

In Figs. **??** we show lines where the constraint on the coupling corresponds to the coupling strength that would reproduce the correct DM density if DM is a thermal relic of the early universe. For points above the line, the LHC constraints naively rule out the couplings leading to the correct relic density. Below this line the relic density coupling is still allowed.

In this scenario, the measured abundance is approximately related to the unknown self-annihilation cross-section via

$$\Omega_{\mathrm{DM}}h^2 \simeq \frac{2 \times 2.4 \times 10^{-10}\,\mathrm{GeV}^{-2}}{\langle \sigma v \rangle_{\mathrm{ann}}}. \tag{5.1}$$

This is used with measurements of the DM abundance by Planck, $\Omega_{\mathrm{DM}}^{\mathrm{obs}}h^2 = 0.1199 \pm 0.0027$ [36], to find $\langle \sigma v \rangle_{\mathrm{ann}} \simeq 4.0 \times 10^{-9}\,\mathrm{GeV}^{-2}$ for thermal relic DM. This relation is only approximately accurate, and so we use the Micromegas code [51] to determine the coupling strength leading to the correct relic density for each model. We verified this technique against the semi-analytic technique outlined in e.g. Ref. [37].

If the DM mass lies at the electroweak scale, the thermal relic scenario provides a natural explanation for the observed DM density, and so the coupling strengths leading to the correct relic density are a natural benchmark with which to compare constraints from other DM searches, indicating the scale at which we expect the couplings may lie. However the relic density couplings should by no means be treated as a constraint. If the DM was not produced thermally or if there is some unknown effect which modifies the evolution of the density with temperature, then these relations break down. Further, even if DM is a thermal relic, then the relationship no longer holds if there are other annihilation channels not taken into account, or if there are other beyond-SM particles contributing to the DM abundance.

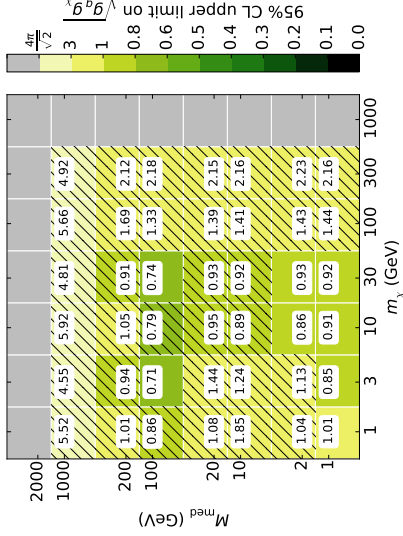### 5.2 Comparison with Direct Detection Constraints

Normally DD is better for vector and LHC is better for Axial vector, but in our case DD is better in both cases until you get to around $m_{\mathrm{DM}} = 5$ GeV at which point our interpolation has broken down.

5.3 Discussion
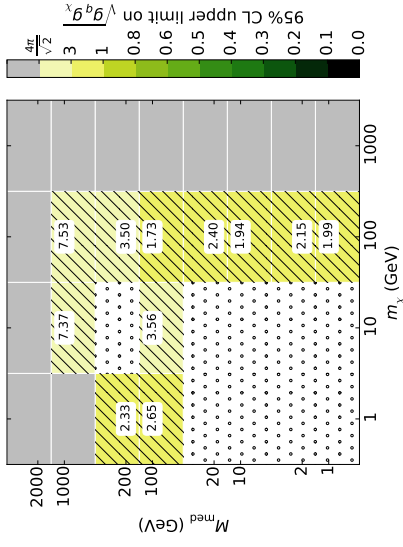
- Comparison to direct mediator searches: dijet gives strongest constraints on mediator especially for small r. Missing ET still good for large M but in this region EFT is fine

- Comparison to non-grid searches, e.g. McCullough et al

- Comparison to grid searches e.g. Zurek et al, Jacques and Nordstrom
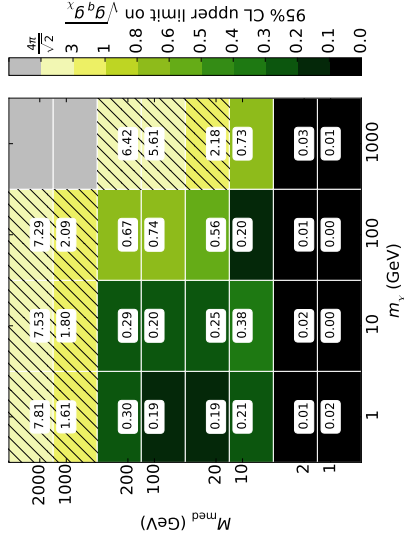
MonoX searches dominate.
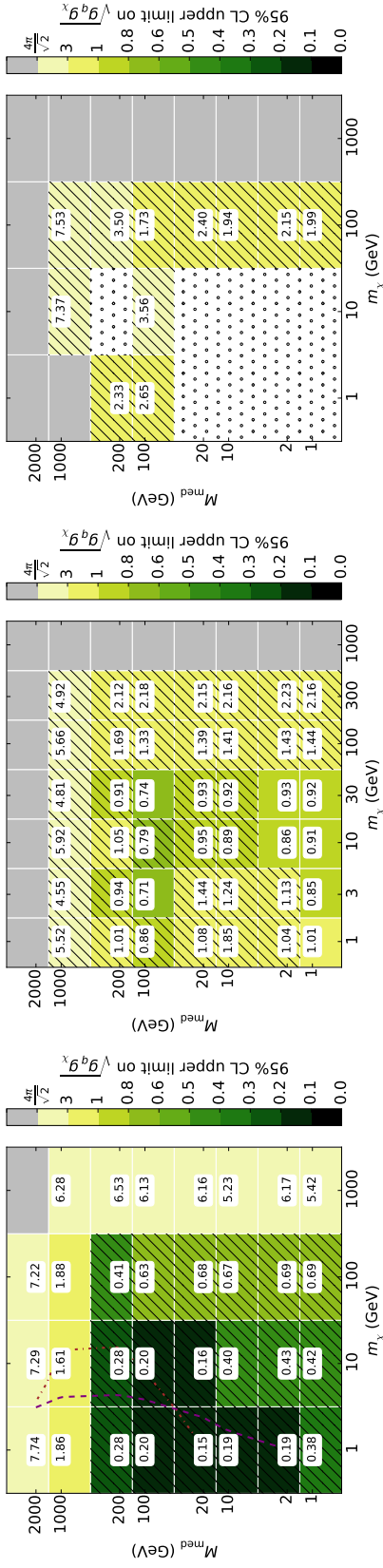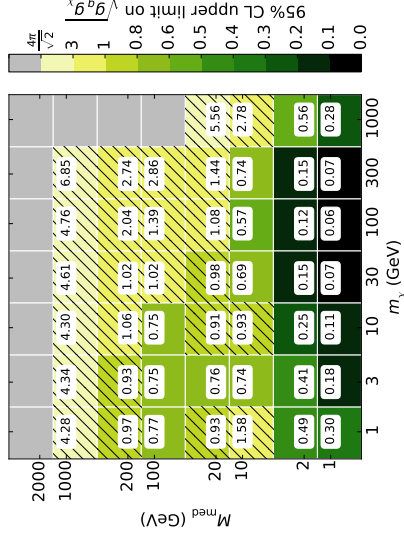
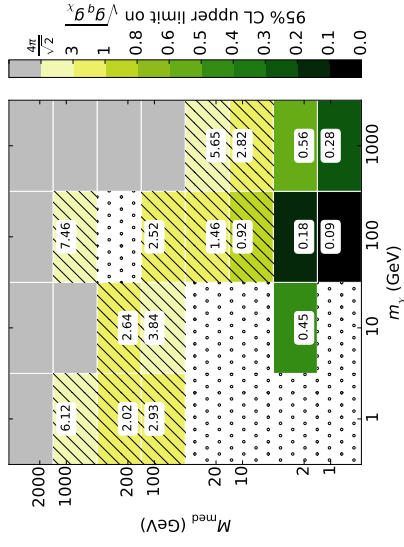(a) sV model, $g_q/g_\chi = 0.5$, mono-jet channel.   (b) sV model, $g_q/g_\chi = 0.5$, mono-Z channel.   (c) sV model, $g_q/g_\chi = 0.5$, mono-W/Z channel.

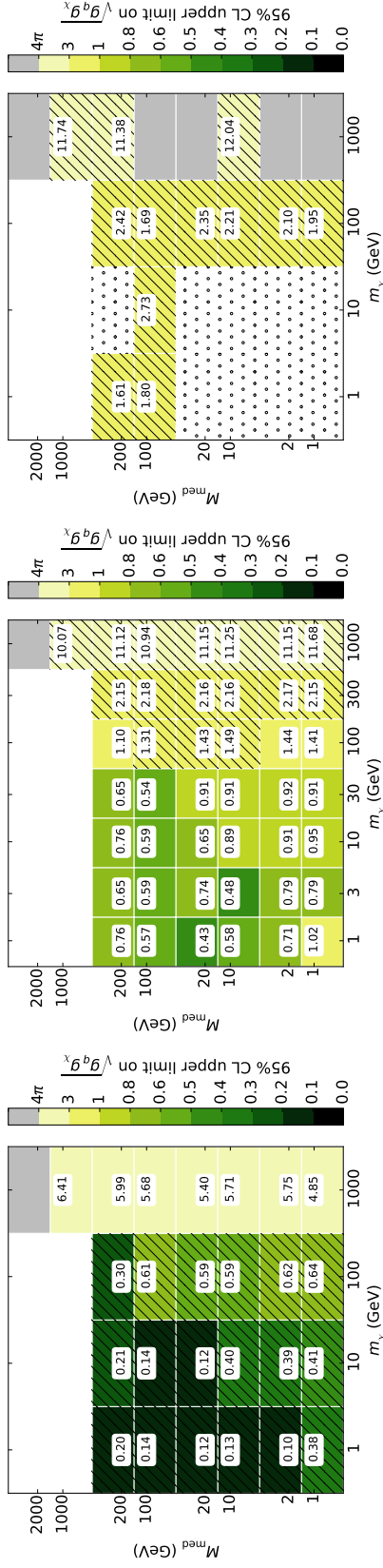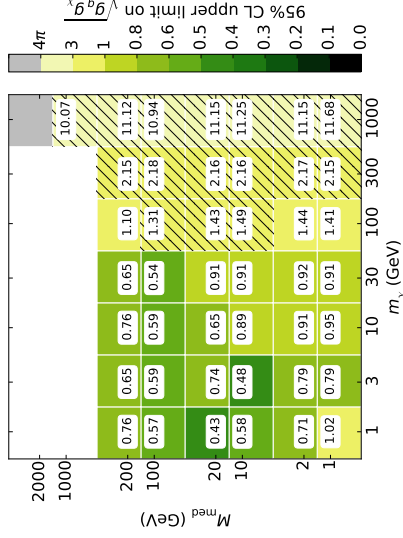(d) sA model, $g_q/g_q = 0.5$, mono-jet channel.   (e) sA model, $g_q/g_\chi = 0.5$, mono-Z channel.   (f) sA model, $g_q/g_\chi = 0.5$, mono-W/Z channel.
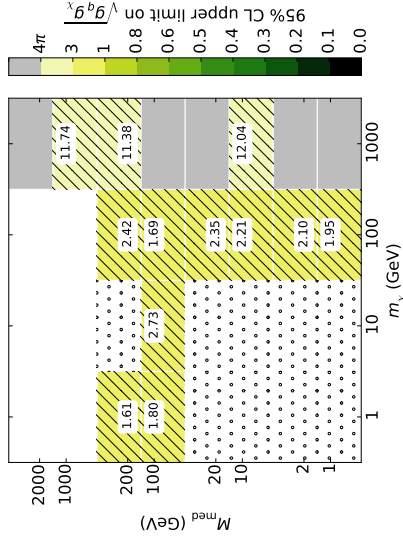
Figure 3: Upper limits on the coupling for the s-channel models in the mono-jet (left), mono-Z (centre) and mono-W/Z (right) channels, for $g_\chi/g_q = 0.5$. The grey region represents the phase space where no meaningful limit was obtained. The hatched region represents a limit which leads to a width greater than $M_{\rm med}/2$, so the validity of the calculation begins to fail. The dotted region represents phase space where insufficient statistics were available.
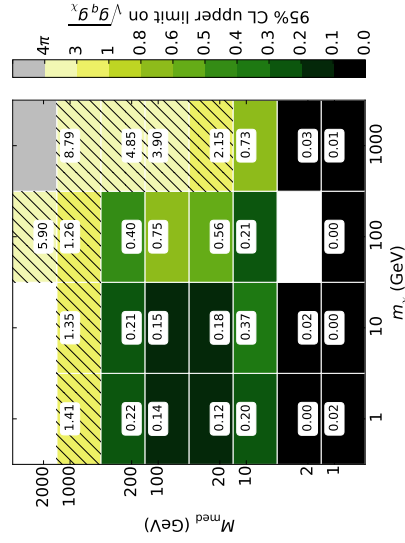
– 16 –

Figure 4: Upper limits on the couplings for the *s*-channel models in the mono-jet (left), mono-*Z* (centre) and mono-*W/Z* (right) channels, for $g_\chi/g_q = 1$. Refer to fig. 3 for details.

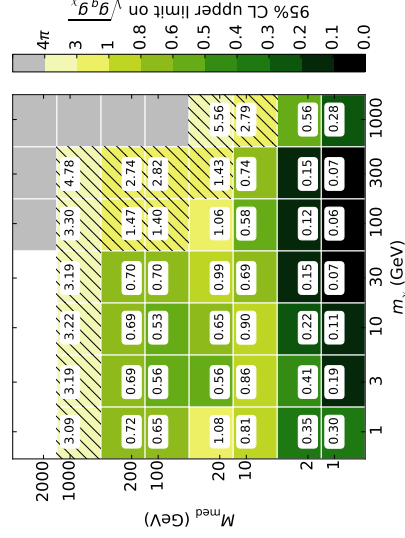(a) sV model, $g_q/g_\chi = 1$, mono-jet channel.

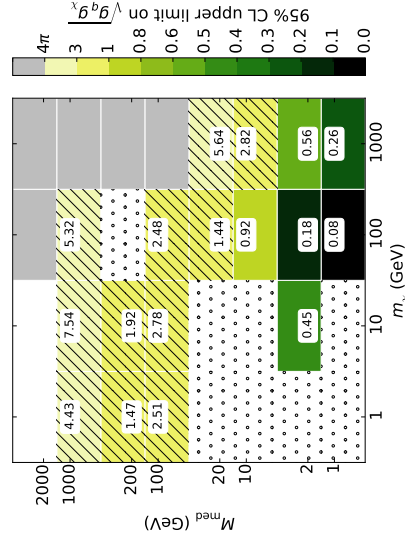(b) sV model, $g_q/g_\chi = 1$, mono-*Z* channel.

(c) sV model, $g_q/g_\chi = 1$, mono-*W/Z* channel.
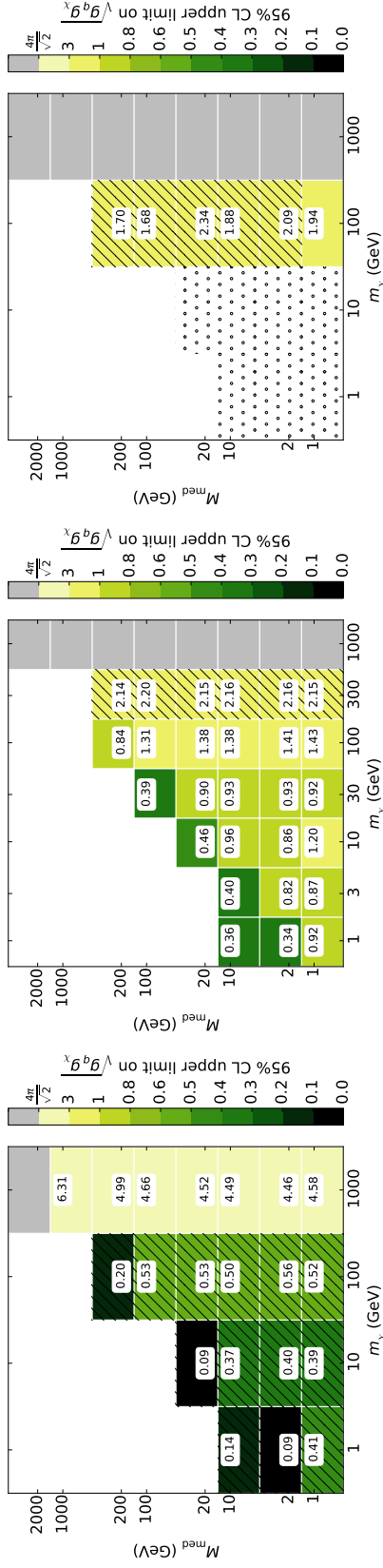
(d) sA model, $g_q/g_\chi = 1$, mono-jet channel.

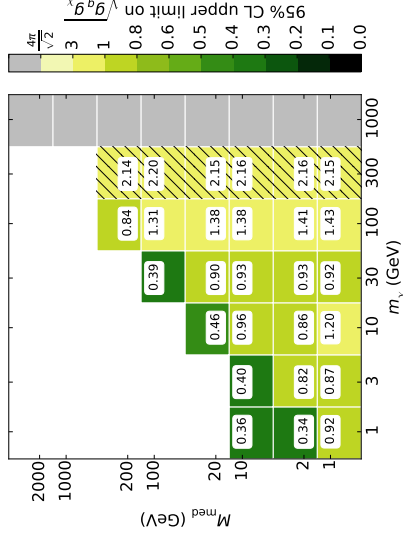(e) sA model, $g_q/g_\chi = 1$, mono-*Z* channel.

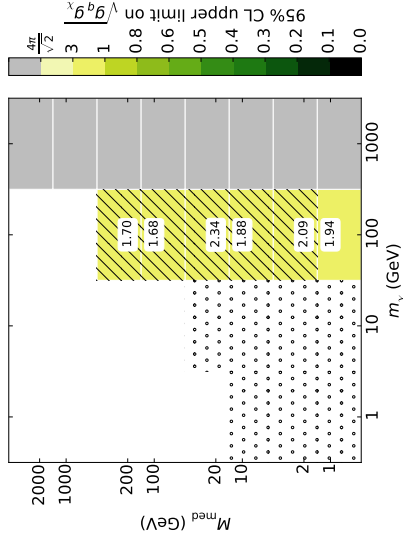(f) sA model, $g_q/g_\chi = 1$, mono-*W/Z* channel.

Figure 5: Upper limits on the coupling for the s-channel models in the mono-jet (left), mono-Z (centre) and mono-W/Z (right) channels, for $g_\chi/g_q = 2$. Refer to fig. 3 for details.
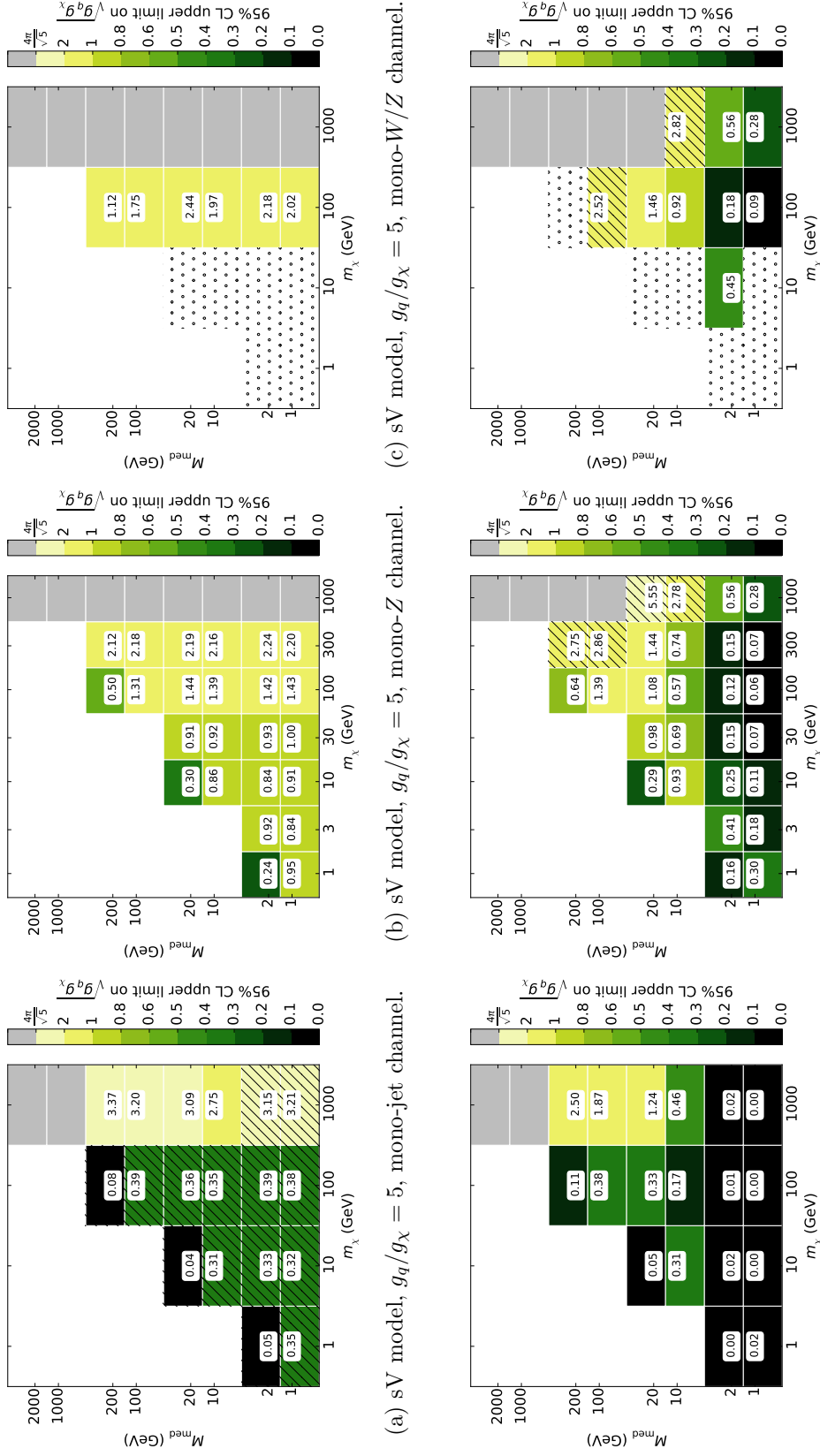
Figure 6: Upper limits on the coupling for the s-channel models in the mono-jet (left), mono-Z (centre) and mono-W/Z (right) channels, for $g_\chi/g_q = 5$. Refer to fig. 3 for details.
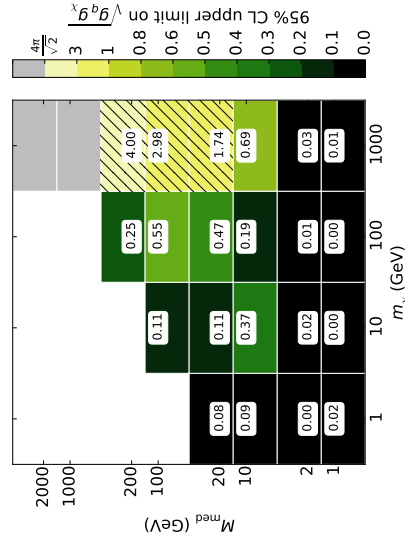
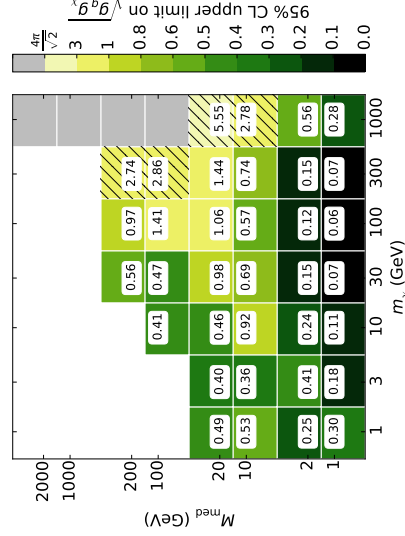(a) sV model, $g_q/g_\chi = 5$, mono-jet channel.

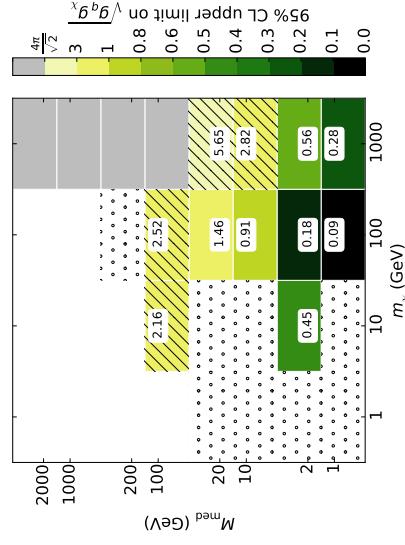(b) sV model, $g_q/g_\chi = 5$, mono-Z channel.

(c) sV model, $g_q/g_\chi = 5$, mono-W/Z channel.

(d) sA model, $g_q/g_\chi = 5$, mono-jet channel.

(e) sA model, $g_q/g_\chi = 5$, mono-Z channel.

(f) sA model, $g_q/g_\chi = 5$, mono-W/Z (right)

(a) sV model, $g_q/g_\chi = 0.2$, mono-jet channel.   (b) sA model, $g_q/g_\chi = 0.2$, mono-jet channel.

Figure 7: Upper limits on the coupling for the s-channel models in the mono-jet channel, for $g_\chi/g_q = 0.2$. Refer to fig. 3 for details.

(a) tS model, mono-Z channel.   (b) tS model, mono-W/Z channel.

Figure 8: Upper limits on the coupling $g_{q\chi}$ for the t-channel model in the mono-Z (left) and mono-W/Z (right) channels. Refer to fig. 3 for details.
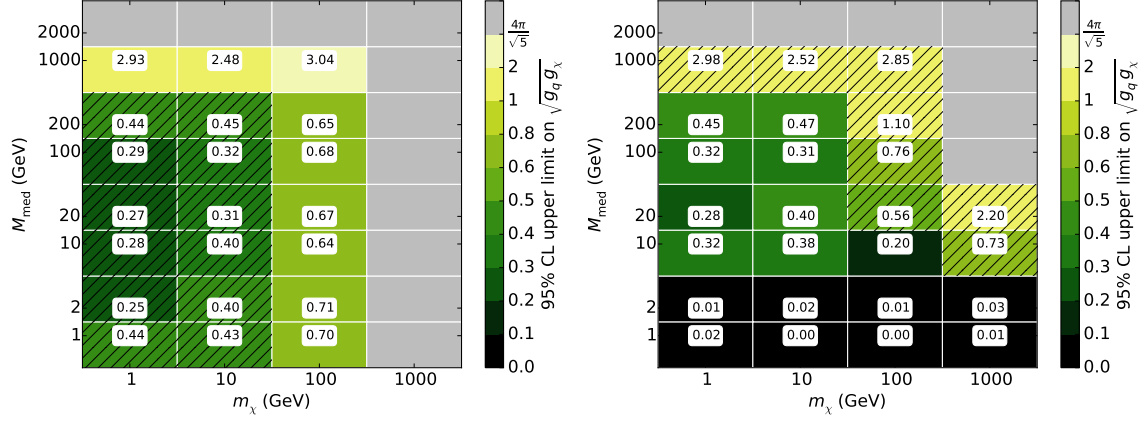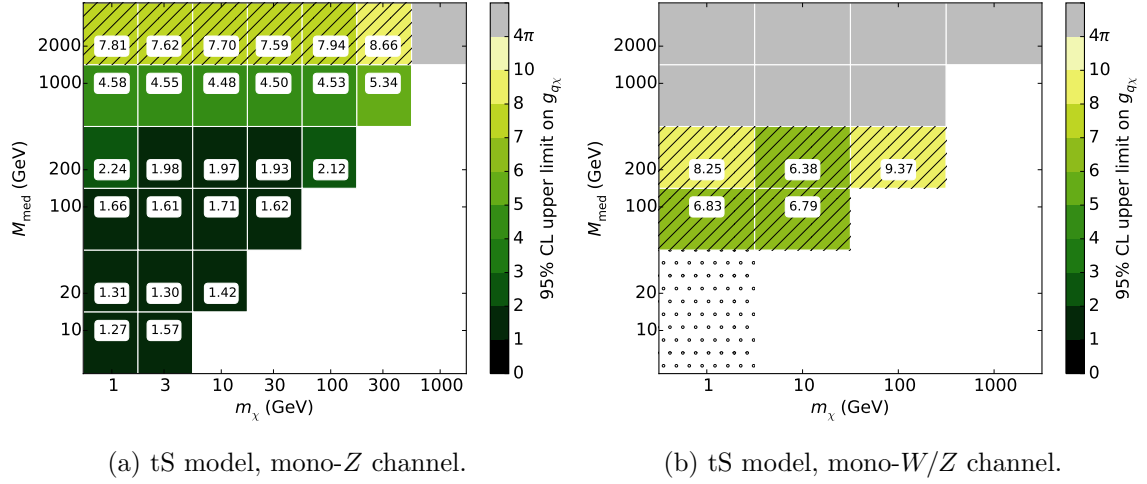
6 Acknowledgements

A Limit setting strategy

In this appendix we present a summary of the procedure employed to calculate the 95% confidence level (CL) limits on the coupling parameter $\sqrt{g_q g_\chi}$, where this parameter can be replaced with $g_{q\chi}$ for the tS model, and $M_\star$ in the validation of the mono-jet analysis.

A.1 Nominal Values

For each simplified model, the nominal value for the observed limit on the cross-section for the process $pp \to \mathrm{X} + \chi\bar{\chi}$ is calculated using the formula:

$$\sigma_{obs}^{lim}(pp \to \mathrm{X} + \chi\bar{\chi}) = \frac{N_{obs}}{\mathcal{L} \times \mathcal{A} \times \epsilon} \tag{A.1}$$

where N_{obs} is a calculated 95% CL upper limit on the number of signal events in the channel and signal region of interest; it is a model-independent quantity. $\mathcal{L}$ is the integrated luminosity, $\mathcal{A}$ is the acceptance (the fraction of signal events passing the channel/SR-specific selection criteria) and ϵ is the efficiency of the ATLAS detector for selecting channel/SR-specific signal events. For all channels the total luminosity is 20.3 fb^{-1} and $\mathcal{A} \times \epsilon$ is regarded as a single variable.

In the following discussion, $\sqrt{g_q g_\chi}$ is assumed to also represent $g_{q\chi}$ from the tS model.

The nominal value for the observed limit Y, where Y is the suppression scale $M_\star$ in the validation of the mono-jet analysis, *or* the coupling values $\sqrt{g_q g_\chi}$ in the general case, is then calculated using

$$Y_{obs}^{lim} = Y^{gen} \left(\frac{\sigma_{obs}^{lim}}{\sigma^{gen}} \right)^{\frac{1}{4}} . \tag{A.2}$$

(Note: this section needs to be re-written to account for the on-shell case as well.)

The signal region in each case is chosen based on where the best 'expected' limit exists, where that limit is calculated assuming that exactly the expected SM background is observed.

A.2 Uncertainty Estimation

Our nominal limits on $M_\star$, $\sigma(pp \to X + \chi\bar{\chi})$ and $\sqrt{g_q g_\chi}$ rely on both σ_{gen} and $\mathcal{A} \times \epsilon$ and so are subject to systematic uncertainties which derive from our choice of MC generation procedure. For our MC samples, there are three key sources of systematic uncertainty: the factorisation and renormalisation scales, the strong coupling constant (α_s) and the parton distribution function (PDF).

Firstly, the factorisation and renormalisation default scales are varied simultaneously by factors of 2 ('up') and 0.5 ('down'). The systematic effects of the strong coupling constant and the PDF are difficult to separate and so are treated in tandem. We assume that the systematic uncertainty introduced by α_s at matrix-element level is negligible when compared to the PDF uncertainties, as demonstrated to be valid in Ref. [42]. The variation

main systematic sources	PDF/tune	factorisation and renormalisation scales	matching scale (mono-jet only)
variation 'up'	NNPDF2.1LO + Monash tune	2	160 GeV
nominal	MSTW2008lo68cl + ATLAS UE AU2-MSTW2008LO	1	80 GeV
variation 'down'	CTEQ6L1 + ATLAS UE AU2-CTEQ6L1	0.5	40 GeV

Table 5: The sources of systematic uncertainty considered in this analysis. Each point in phase space is varied up or down by one of these sources, and the systematic uncertainty is taken to be the average difference in $\mathcal{A}'$ from the nominal value.

of α_s in conjunction with a PDF is done with the use of specific tunes in PYTHIA , which we change simultaneously with the PDF choice to estimate the uncertainty on $\Delta\sigma_{gen}$. The nominal choices of PDF and tune are varied 'up' to NNPDF2.1LO PDF + Monash tune, and 'down' to CTEQ6L1 PDF and ATLAS UE AU2-CTEQ6L1 tune. Millie: put discussion of matching scale systematic here. These systematic uncertainty sources are summarised in table 5.

Following eqns. A.1 and A.2, the relative uncertainty in the limit on $\sqrt{g_q g_\chi}$ (or on $M_\star$) is given by (to be updated with on-shell case also)

$$\frac{\Delta\sqrt{g_q g_\chi}}{\sqrt{g_q g_\chi}} = \frac{1}{4}\sqrt{\left(\frac{\Delta\sigma_{gen}}{\sigma_{gen}}\right)^2 + \left(\frac{\Delta(\mathcal{A}\times\epsilon)}{\mathcal{A}\times\epsilon}\right)^2 + \left(\frac{\Delta\mathcal{L}}{\mathcal{L}}\right)^2} \qquad (A.3)$$

For $P = \sigma_{gen}, \mathcal{A}\times\epsilon$, the relative error $\Delta P/P$ is found by summing in quadrature the separate sources of uncertainty, according to

$$\left(\frac{\Delta P}{P}\right)^2_{\text{total}} = \left(\frac{\Delta P}{P}\right)^2_{\text{scale}} + \left(\frac{\Delta P}{P}\right)^2_{\text{PDF+tune}} + \left(\frac{\Delta P}{P}\right)^2_{\text{matching}} \qquad (A.4)$$

where ΔP is taken as the average distance from the nominal value P when the systematic source is varied up and down. The statistical uncertainty is taken into account rather conservatively by using the 95%CL *lower* limit on $\mathcal{A}\times\epsilon$ as calculated with the Wald approximation, i.e. $\mathcal{A}\times\epsilon \rightarrow (\mathcal{A}\times\epsilon) - \Delta(\mathcal{A}\times\epsilon)$. The uncertainty on the luminosity is less than 3%, so is considered to be negligible in comparison to other systematic sources.

B Validation of signal simulation and event selection procedures

B.1 Monojet Channel

The MC generation and signal selection procedures for the mono-jet channel are validated via reproduction of the ATLAS limits on $M_\star \equiv M_{\rm med}/\sqrt{g_q g_\chi}$, for the s-channel vector simplified model. A comparison of SR7 limits for a representative sample of mediator masses with $m_\chi = 50$ GeV, $\Gamma = M/8\pi$ and $\sqrt{g_q g_\chi} = 1$ is presented in Table 6. In general, good agreement is observed between the ATLAS and reproduced limits, with a maximum difference (with respect to the ATLAS limit) of $<23\%$. We note that a discrepancy of a few percent is expected and allowed for three reasons. Firstly, the MC generation procedure employed in this analysis does not include a full simulation of the ATLAS detector. Instead, reconstruction effects are simulated by applying a Gaussian smearing of the jet $p_{\rm T}$ by a conservative factor of 5%. Next, the matching procedure employed in this analysis (and discussed in detail in Section 3.1.1) is largely simplified. This introduces a substantial uncertainty when compared to the matching procedure utilised by the ATLAS mono-jet group. For example, where the ATLAS group observe a maximum matching scale uncertainty of 5% for events with $E_{\rm T}^{\rm miss}$ above 350 GeV, we observe an uncertainty of $\sim 30\%$. Lastly, the 95% CL uncertainties on $M_\star$ for this work are estimated in a non-identical fashion to that used in the ATLAS analysis. In particular, where the ATLAS limits are estimated using the HistFitter package, we use the approach described in appendix A. As our results are consistently more conservative than those of the ATLAS analysis, we consider this approach acceptable.

M [TeV]	$M_\star^{\rm ATLAS95}$ [GeV]	$M_\star^{95}$ [GeV]	Difference [%]
0.05	91	89	2.16
0.3	1151	1041	7.3
0.6	1868	1535	11.8
1	2225	1732	12.0
3	1349	1072	6.8
6	945	769	8.5
10	928	724	10.6
30	914	722	9.6

Table 6: Comparison of the 95% CL upper limits on $M_\star$ from this work ($M_\star^{95}$) and from the ATLAS mono-jet analysis ($M_\star^{\rm ATLAS,95}$) [41]. The values shown in the second and third columns are for the processes $pp \to j\chi\bar{\chi}$ and $pp \to jj\chi\bar{\chi}$ for the s-channel vector mediator model with $m_\chi = 50$ GeV, $\Gamma = M/8\pi$, $\sqrt{g_q g_\chi} = 1$ and QCUT = 80 GeV.

B.2 Mono-Z Channel

The ATLAS mono-Z analysis result includes an upper limit on the coupling $g_{q\chi}$ for a t-channel simplified model that is very similar to the model investigated here, and so is used for validating our signal generation and selection procedure. The most significant

m_χ [GeV]	M_{med} [GeV]	$g_{q\chi}^{95\%\mathrm{CL}}$ (ATLAS)	$g_{q\chi}^{95\%\mathrm{CL}}$ (this work)	Difference [%]
10	200	1.9	2.0	5.3
	500	2.8	3.2	14.3
	700	3.5	4.4	25.7
	1000	4.5	5.2	15.6
200	500	3.4	4.0	17.6
	700	4.2	4.5	7.1
	1000	5.2	5.3	1.9
400	500	5.5	5.7	3.6
	700	6.1	6.5	6.6
	1000	7.2	7.4	2.8
1000	1200	23.3	24.1	3.4

Table 7: Comparison of the upper limit on $g_{q\chi}$ from the ATLAS analysis [47] and this work.

541 differences are in the number of mediating particles — the ATLAS model includes just
542 two mediators (*up*- and *down*-type) compared to our six — and in the nature of the DM
543 particle, which is taken to be Majorana. This latter choice does not impact the kinematic
544 behaviour, but does scale the cross section by a simple factor. Additionally, while we use a
545 universal coupling $g_{q\chi}$ to all three quark generations, the analysis used a model which set
546 $g_{t,b\chi} = 0$.

547 Table 7 shows the 95% CL upper limits on $g_{q\chi}$ that we calculate using the same *t*-
548 channel model and our own generation procedure (using the values in table **??**), compared
549 with the limits on this same variable taken from the ATLAS analysis. The difference as a
550 percentage of the ATLAS limit is also shown in the table. We see reasonable agreement;
551 most of the 11 points in parameter space are within 10% of the ATLAS limits, and all are
552 within 26%. Additionally, our results are consistently more conservative, which is to be
553 expected due to the less sophisticated nature of our generation procedure. Similarly to the
554 mono-jet validation, the dominant effects are due to the use of p_{T} smearing applied to the
555 leptons, rather than considering the full reconstruction effects, and the simple systematic
556 treatment that was used with HistFitter.

557 **B.3   Mono-W/Z Channel**

558 Johanna, please put your validation results here.

559 **References**

560 [1] ATLAS Collaboration, *Search for new phenomena with the monojet and missing transverse*
561 *momentum signature using the ATLAS detector in $\sqrt{s} = 7$ TeV proton-proton collisions*,
562 *Phys. Lett. B* (2011), arXiv:1106.5327.

[2] ATLAS Collaboration, *Search for New Phenomena in Monojet plus Missing Transverse Momentum Final States using 10 fb^{-1} of pp collisions at $\sqrt{s}$=8 TeV with the ATLAS detector at the LHC*, 2012, ATLAS-CONF-2012-147.

[3] CMS Collaboration, *Search for new physics in monojet events in pp collisions at $\sqrt{s} = 8$ TeV*, 2013, CMS-PAS-EXO-12-048.

[4] M. R. Buckley, *Using Effective Operators to Understand CoGeNT and CDMS-Si*, Phys.Rev. D 88, 055028 (2013), arXiv:1308.4146.

[5] J. Abdallah et al., *Search for new phenomena with mono-jet plus missing transverse energy signature in pp collisions at $\sqrt{s}$=8 TeV with the ATLAS detector*, 2012, ATL-COM-PHYS-2012-1211.

[6] N. Bell et al., *Searching for Dark Matter at the LHC with a Mono-Z*, Phys.Rev. D 86, 096011 (2012), arXiv:1209.0231.

[7] N. Zhou, D. Berge, and D. Whiteson, *Mono-everything: combined limits on dark matter production at colliders from multiple final states*, Phys.Rev. D 87, 095013 (2013), arXiv:1302.3619.

[8] M. Cahill-Rowley et al., *Complementarity and Searches for Dark Matter in the pMSSM*, SLAC-PUB-15450 (2013), arXiv:1305.6921.

[9] ATLAS Collaboration, *Further search for supersymmetry at $\sqrt{s} = 7$ TeV in final states with jets, missing transverse momentum and isolated leptons with the ATLAS detector*, Phys.Rev. D 86, 092002 (2012), arXiv:1208.4688.

[10] ATLAS Collaboration, *Search for squarks and gluinos with the ATLAS detector in final states with jets and missing transverse momentum using 4.7 fb^{-1} of $\sqrt{s} = 7$ TeV proton-proton collision data*, Phys.Rev. D 87, 012008 (2013), arXiv:1208.0949.

[11] ATLAS Collaboration, *Search for pair-produced third-generation squarks decaying via charm quarks or in compressed supersymmetric scenarios in pp collisions at $\sqrt{s} = 8$ TeV with the ATLAS detector*, Phys.Rev. D 90, 052008 (2014), arXiv:1407.0608.

[12] ATLAS Collaboration, *Search for squarks and gluinos with the ATLAS detector in final states with jets and missing transverse momentum using $\sqrt{s} = 8$ TeV proton-proton collision data*, JHEP 09 (2014) 146, arXiv:1405.7875.

[13] H. Dreiner et al., *Contact Interactions Probe Effective Dark Matter Models at the LHC*, Europhys.Lett. (2013), arXiv:1303.3348.

[14] J. Goodman et al., *Gamma Ray Line Constraints on Effective Theories of Dark Matter*, Nucl.Phys. (2011), arXiv:1009.0008.

[15] G. Busoni et al., *On the Validity of the Effective Field Theory for Dark Matter Searches at the LHC*, Phys.Lett. (2014), arXiv:1307.2253.

[16] G. Busoni et al., *On the Validity of the Effective Field Theory for Dark Matter Searches at the LHC, Part II: Complete Analysis for the s-channel*, JCAP 1406:060 (2014), arXiv:1402.1275.

[17] G. Busoni et al., *On the Validity of the Effective Field Theory for Dark Matter Searches at the LHC Part III: Analysis for the t-channel*, JCAP 09 (2014) 022, arXiv:1405.3101.

[18] Oliver Buchmueller, Matthew J. Dolan, Sarah A. Malik and Christopher McCabe,

Characterising dark matter searches at colliders and direct detection experiments: Vector mediators, 2014, arXiv:1407.8257.

[19] J. Kumar and D. Marfatia. *Matrix element analyses of dark matter scattering and annihilation*, *Phys.Rev.* (2013), arXiv:1305.1611.

[20] G. Jungman et al., *Supersymmetric dark matter*, *Phys.Rept.* (1996).

[21] P. J. Fox et al., *Missing Energy Signatures of Dark Matter at the LHC*, *Phys.Rev.* (2012), arXiv:1109.4398.

[22] P. J. Fox, R. Harnik, R. Primulando, and C-T. Yu, *Taking a Razor to Dark Matter Parameter Space at the LHC*, *Phys.Rev.* (2012), arXiv:1203.1662.

[23] M. Papucci, A. Vichi, and K. M. Zurek, *Monojet versus rest of the world I: t-channel Models*, *JHEP* (2014), arXiv:1402.2285.

[24] Y. Bai, P. J. Fox, and R. Harnik, *The Tevatron at the Frontier of Dark Matter Direct Detection*, *JHEP* (2010), arXiv:1005.3797.

[25] J. Goodman et al., *Constraints on Dark Matter from Colliders*, *Phys.Rev.* D 82, 116010 (2010), arXiv:1008.1783.

[26] P. J. Fox, R. Harnik, J. Kopp, and Y. Tsai, *LEP Shines Light on Dark Matter*, *Phys.Rev.* (2011), arXiv:1103.0240.

[27] M. L. Graesser, I. M. Shoemaker, and L. Vecchi, *A Dark Force for Baryons*, 2011, arXiv:1107.2666.

[28] H. An and F. Gao, *Fitting CoGeNT Modulation with an Inelastic, Isopin-Violating Z'* *Model*, 2011, arXiv:1108.3943.

[29] CMS Collaboration, *Search for narrow resonances using the dijet mass spectrum in pp collisions at $\sqrt{s} = 8 TeV$*, *Phys.Rev.* (2013), arXiv:1302.4794.

[30] ATLAS Collaboration, *Search for high-mass resonances decaying to dilepton final states in pp collisions at $s^{**}(1/2) = 7$-TeV with the ATLAS detector*, *JHEP* (2012), arXiv:1209.2535.

[31] P. Harris, V. V. Khoze, M. Spannowsky and C. Williams, *Constraining Dark Sectors at Colliders: Beyond the Effective Theory Approach*, *Phys.Rev.* (2015), arXiv:1411.0535.

[32] CMS Collaboration. *Search for new physics in monojet events in pp collisions at $\sqrt{s} = 8$ TeV*, 2013, CMS-PAS-EXO-12-048.

[33] ATLAS Collaboration. *Search for New Phenomena in Monojet plus Missing Transverse Momentum Final States using 10 fb^1 of pp collisions at $\sqrt{s} = 8$ TeV with the ATLAS detector at the LHC*, 2012, ATLAS-CONF-2012-147.

[34] J. Kumar and D. Marfatia, *Matrix element analyses of dark matter scattering and annihilation*, *Phys.Rev.* (2013), arXiv:1305.1611.

[35] D. Alves et al., *Simplified Models for LHC New Physics Searches*, *J.Phys.* (2012), arXiv:1105.2838.

[36] P. A. R. Ade *et al.* [Planck Collaboration], Astron. Astrophys. **571**, A16 (2014) [arXiv:1303.5076 [astro-ph.CO]].

[37] G. Busoni, A. De Simone, T. Jacques, E. Morgante and A. Riotto, *Making the Most of the Relic Density for Dark Matter Searches at the LHC 14 TeV Run*, *JCAP* 03 (2015) 022, arXiv:1410.7409.

[38] CMS Collaboration. *Search for new physics in monojet events in pp collisions at $\sqrt{s} = 8$ TeV*, 2013, CMS-PAS-EXO-12-048.

[39] ATLAS Collaboration. *Search for New Phenomena in Monojet plus Missing Transverse Momentum Final States using 10 fb^1 of pp collisions at $\sqrt{s} = 8$ TeV with the ATLAS detector at the LHC*, 2012, ATLAS-CONF-2012-147.

[40] ATLAS Collaboration. *Further search for supersymmetry at $\sqrt{s} = 7$ TeV in final states with jets, missing transverse momentum and isolated leptons with the ATLAS detector, Phys.Rev.* (2012), arXiv:1208.4688.

[41] ATLAS Collaboration. *Search for new phenomena in final states with an energetic jet and large missing transverse momentum in pp collisions at $\sqrt{s} = 8$ TeV with the ATLAS detector*, 2015, arXiv:1502.01518

[42] S. Schramm, *Searching for Dark Matter with the ATLAS Detector in Events with an Energetic Jet and Large Missing Transverse Momentum*, 2015, CERN-THESIS-2015-038.

[43] A. Cooper-Sarkar. *PDFs for the LHC*, 2011, arXiv:1107.5170.

[44] ATLAS Collaboration. *Search for dark matter candidates and large extra dimensions in events with a jet and missing transverse momentum with the ATLAS detector*, 2013, CERN-PH-EP-2012-210, arXiV:1210.4491.

[45] P. J. Fox et al. *Missing Energy Signatures of Dark Matter at the LHC, Phys. Rev.*, 2012.

[46] N. Bell, J. Dent, T. Jacques, and T. Weiler. *W/Z Bremsstrahlung as the Dominant Annihilation Channel for Dark Matter, Phys. Rev.*, 2011.

[47] ATLAS Collaboration. *Search for dark matter in events with a Z boson and missing transverse momentum in pp collisions at $\sqrt{s} = 8$ TeV with the ATLAS detector, Phys.Rev.D* **90** (2014) 012004, arXiv:1404.0051.

[48] J. Alwall /emphet al.. *The automated computation of tree-level and next-to-leading order differential cross sections, and their matching to parton shower simulations, JHEP07* (2014) 079, arXiv:1405.0301.

[49] A. D. Martin, W. J. Stirling, R. S. Thorne, G. Watt, *Parton distributions for the LHC, Eur.Phys.J.C63*, (2009), 189-285, arXiv:0901.0002.

[50] ATLAS Collaboration. *Summary of ATLAS Pythia8 tunes*, 2012, ATL-PHYS-PUB-2012-003.

[51] G. Blanger, F. Boudjema, A. Pukhov and A. Semenov, Comput. Phys. Commun. **192**, 322 (2015) doi:10.1016/j.cpc.2015.03.003 [arXiv:1407.6129 [hep-ph]].

[52] D. Abercrombie et al. *Dark Matter Benchmark Models for Early LHC Run-2 Searches: Report of the ATLAS/CMS Dark Matter Forum*, arXiv:1507.00966.

[53] M. Baak et al. *HistFitter software framework for statistical data analysis, Eur.Phys.J.C* (2015), arXiv:1410.1280.

[54] J. Abdallah et al. *Simplified Models for Dark Matter Searches at the LHC, Phys. Dark Uni.* 9-10 (2015) 8-23, arXiv:1506.03116.

[55] J. Abdallah et al. *Simplified Models for Dark Matter and Missing Energy Searches at the LHC*, (2014), arXiv:1409.2893.

[56] T. Jacques and K. Nordstrom, *Mapping monojet constraints onto Simplified Dark Matter Models, JHEP* 06 (2015) 142, arXiv:1502.05721.